Geothermal Resources Council 2011 Annual Meeting

Investigation of Stimulation-Response Relationships for Complex Fracture Systems in Enhanced Geothermal Reservoirs

Fu, P., Johnson, S.M. and Carrigan, C.R.
Lawrence Livermore National Laboratory, Livermore, CA, U.S.A.

ABSTRACT: Hydraulic fracturing is currently the primary method for stimulating low-permeability geothermal reservoirs and creating Enhanced (or Engineered) Geothermal Systems (EGS) with improved permeability and heat production efficiency. Complex natural fracture systems usually exist in the formations to be stimulated and it is therefore critical to understand the interactions between existing fractures and newly created fractures before optimal stimulation strategies can be developed. Our study aims to improve the understanding of EGS stimulation-response relationships by developing and applying computer-based models that can effectively reflect the key mechanisms governing interactions between complex existing fracture networks and newly created hydraulic fractures. In this paper, we first briefly describe the key modules of our methodology, namely a geomechanics solver, a discrete fracture flow solver, a rock joint response model, an adaptive remeshing module, and most importantly their effective coupling. After verifying the numerical model against classical closed-form solutions, we investigate responses of reservoirs with different preexisting natural fractures to a variety of stimulation strategies. The factors investigated include: the in situ stress states (orientation of the principal stresses and the degree of stress anisotropy), pumping pressure, and stimulation sequences of multiple wells.

Keyword: geothermal; enhanced geothermal system; EGS; hydraulic fracture; discrete fracture flow

1. INTRODUCTION

Hydraulic fracturing is a promising method for stimulating low-permeability geothermal reservoirs and creating Enhanced (or Engineered) Geothermal Systems (EGS) with improved permeability and heat production efficiency (MIT, 2006). Complex natural fracture systems usually exist in the formations to be stimulated, as revealed by mineback experiments and tiltmeter/microseismic mapping (Warpinski et al., 1987; Fisher et al., 2005; King et al., 2008). It is thus critical to understand the interactions between existing fracture systems and newly created fractures in order to develop optimal stimulation strategies. The mechanisms of interactions between existing/natural fractures and propagating new fractures are two-fold. First, new hydraulic fractures can bridge isolated natural fractures and increase the inter-connectivity of the existing fracture system, thereby enhancing formation permeability. On the other hand, the existing fracture system can greatly affect the creation of new hydraulic fractures by bridging, diverting, or impeding their propagation. In contrast to the complex nature of interactions between fractures, existing analytical and numerical models (see Adachi et al., 2007 for a review) have mostly focused on the behavior of a single fracture, assuming that the primary mechanism of permeability enhancement is the conductivity provided by a single straight fracture driven by hydraulic pressure.

The primary objective of this work, is to develop realistic computer-based models of EGS stimulation-response scenarios involving hydraulic stimulation of fracture systems in hard rock formations where a pre-existing fracture network may be present along with regional stress and temperature distributions. To this end, we have developed a two-dimensional (2D) numerical model that couples geomechanics modeling and discrete fracture flow simulation and is capable of handling fractures with arbitrary geometries based upon existing simulation capabilities of the Lawrence Livermore National Laboratory.

The methodologies employed by this numerical simulator have been reported in our previous publications (Fu et al., 2011a; 2011b) and is only briefly described in Section 2. This paper primarily focuses on the application of this numerical test-bed code to study the responses of naturally fractured reservoirs to a variety of hydraulic stimulation scenarios

2. NUMERICAL TEST BED

2.1. General Approach

Hydraulic fracturing is essentially a process of interaction between pressurized fluid in discrete fractures and the rock matrix, governed by, among others, the following physical mechanisms.

- Fluid flow in fractures due to pressure gradient;
- The deformation of the rock under the pressure of the fluid and other external loads;
- The variation of fracture aperture width (which dictates the conductivity of the fractures) owing to the deformation of the rock body; and
- The fracturing of rock.

To reasonably simulate this process, our numerical model consists of and tightly couples the following modules:

- A solid (geomechanics) solver, providing the non-local mechanical responses of the rock matrix;
- A flow simulator, solving the fluid flow in inter-connected fracture networks;
- An adaptive remeshing module, generating new meshes for both the solid solver and the flow solver as fractures are created; and
- A rock joint model, determining hydraulic aperture sizes based on mechanical responses of the rock matrix as well as mechanical responses local to the fracture discontinuities.

The basic principles of these modules are briefly described in the subsequent sections. The exchange of information between these individual modules in fully coupled analysis is shown in Figure 1.

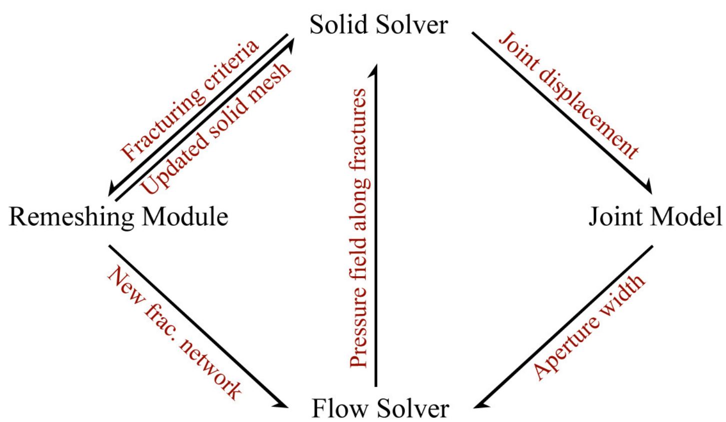

Figure 1 Important modules of the hydraulic fracturing simulator and information exchange between them in coupled simulations.

2.2. FEM Solid Solver

The core of the solid mechanics solver is an explicitly integrated finite element engine utilizing six-node triangular elements. A standard central-difference explicit time integration method is used, so the solver is inherently of a dynamic nature. To manage the high computational cost associated with the coupling of the solid and the flow solvers, some inherent features of the hydraulic fracturing process are exploited, such as using a small deformation formulation and employing a relatively high damping ratio to stabilize the simulations, thanks to the quasi-static nature of this process.

2.3. Solver for Discrete Flow Network

Fluid flow in rock fractures is idealized as laminar flow between two parallel plates with variable distances with respect to both time and location. The governing equations are:

$$\frac{\partial q}{\partial l} + \frac{\partial w}{\partial t} = 0 \qquad (1)$$

$$\kappa \frac{\partial P}{\partial l} = -q \qquad (2)$$

$$\kappa = \frac{w^3}{12\mu} \qquad (3)$$

where l and t represent the length along the fracture and time, respectively; q is the local flow rate in the fracture at a given cross-section; w is the local aperture size, namely the distance between the two rock walls along the fracture; P is the fluid pressure; and κ represents the permeability of the fracture, which is a function of the dynamic viscosity μ of the fluid and the local fracture aperture width w. These equations are solved with a modified finite volume method (FVM). The discrete format of the finite volume method and the boundary conditions to be imposed have been described by Johnson and Morris (2010), and are not repeated here. The flow system is solved using a central-difference explicit integration method, which is compatible with the solution method in the solid solver, enabling their efficient coupling.

2.4. Fracturing Criterion

We use a discrete inter-element cohesive fracture approach similar to the methods proposed by Xu and Needleman (1994) and Camacho and Ortiz (1996). In such an approach, once the fracturing criterion is met at a node in the solid finite element mesh, the cohesive elements are invoked and this node is split, generating new surfaces (lines in 2D) in the solid mesh and new conducting flow channels in the flow mesh, both of which are automatically handled by the adaptive remeshing module. In the current model, the fracturing criterion is based on the tensile stress magnitude along potential fracture paths, namely edges between adjacent solid elements. This "breaking strength" (or the threshold stress value) can be related to the rock toughness and geometrical characteristics of the, using the method of Camacho and Ortiz (1996). In the proposed numerical test bed method, the breaking strength is treated as a parameter subject to sensitivity analysis in order to learn the responses of a variety of rocks with a spectrum of toughnesses to different stimulation scenarios.

2.5. Joint Model

Fractures are treated as mechanical joint elements in the solid solver. The joint model predicts the local mechanical responses of fractures (opening, closing, sliding and dilation) to the deformation and stress states in the rock body, and it also provides information regarding the conductivity (i.e., hydraulic aperture sizes) of the fractures to the flow solver. This simulator uses a discrete element-type contact model to handle the interactions between the rock bodies at the two sides along a fracture. The joint model keeps tracking the locations of the opposing solid elements along a fracture. When they come to contact, a contact stress is applied along the joint, essentially a penalty method. When relative displacement in the tangential direction takes place between these two opposing elements, shear stress is applied and Coulomb's friction law is enforced, making frictional sliding of rocks along the fractures possible. When the two opposing elements separate from each other with a positive distance (δ_n>0) due to the pressurization of the fracture, the following equation (4) is used to calculate the hydraulic aperture.

$$w = \begin{cases} \delta_n & \text{if } \delta_n > w_r \\ w_r & \text{if } \delta_n \le w_r \end{cases} \qquad (4)$$

where w_r is called the "residual" aperture, which represents the residual flow conductivity of a closed fracture (i.e. the fluid pressure is not high enough to overcome the compressive rock stress) due to asperity of the fracture surface. Joint models available in the literature of rock mechanics (Barton et al., 1985) that more realistically consider mechanical and conductive behaviors of joints are being researched in our study and will be implemented in future models. Nevertheless, the current simple model provides the basic capability to take into account the most important mechanisms, namely the opening and closing of fractures due to the variation of fluid pressure.

3. VERIFYING THE NUMERICAL MODEL AGAINT THE KGD MODEL

3.1. The KGD Model

The so-called KGD model deals with a single fracture under the plane-strain assumption driven by a Newtonian fluid at a constant flow rate injected into the well. It was independently developed by Khristianovic and Zheltov (1955), and Geertsma and de Klerk (1969). A closed-form solution is available (Dahi-Taleghani, 2009) to predict the length L of the fracture as a function of injection time t if fluid leak-off is ignored, i.e.

$$L(t) = 0.605\left[\frac{Gq_0^3}{\mu(1-\nu)}\right]^{\frac{1}{6}} t^{\frac{2}{3}} \qquad (5)$$

where G and v are the shear modulus and the Poisson's ratio of the rock body; q_0 is the constant injection flow rate per unit thickness along the well bore direction.

3.2. Numerical Implementation of the KGD Model

In order to verify the numerical model, a simulation is conducted under conditions resembling the assumptions of the KGD model. The core simulation domain has dimensions of 100 m and 120 m in the x and y directions, respectively, and is discretized into 96,000 triangular elements of uniform sizes. The core mesh is then extended to approximately 1,000 m in each direction with larger elements to reduce the effect of the far-field boundaries as shown in Figure 2. "Roller" boundary conditions are applied to all the four edges of the mesh. At the left side boundary this applies a symmetrical condition. Since the KGD model is formulated based on the "net pressure", namely the fluid pressure in excess of the normal stress in the rock acting along the potential fracture direction, no *in situ* stress is applied. The rock body is assumed to have a shear modulus of 8 GPa and Poisson's ratio of 0.25. Water with a dynamic viscosity of 0.001 Pa•s is injected at a flow rate of 10 liters per second per unit thickness normal to the 2D plane.

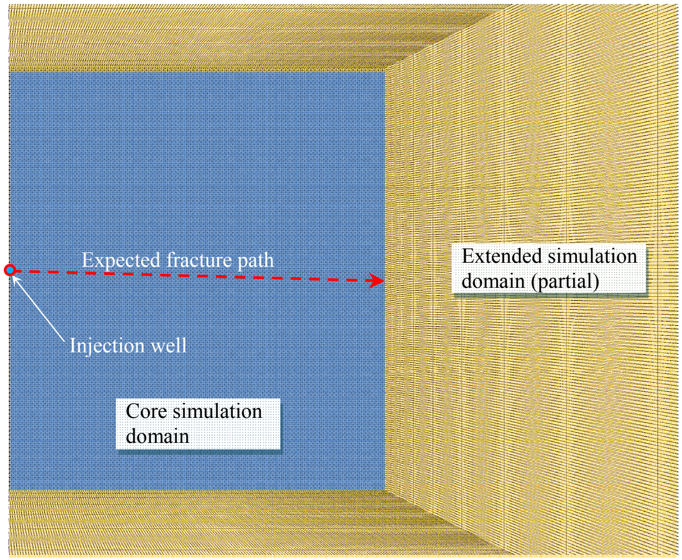

Figure 2 Mesh of the numerical KGD model.

3.3. Simulation Results

The comparison of the hydraulic fracture length *L* as a function of the injection time *t* between the numerical simulation result and the KGD closed-form equation is shown in Figure 3, and a reasonable agreement is achieved, especially when the fracture is relatively long. We performed another simulation with a two times coarser mesh in each dimension and otherwise identical parameters. The results did not show perceivable change with the variation of the mesh sizes, and thus are not shown in the figure. This observation indicates satisfactory convergence of the model.

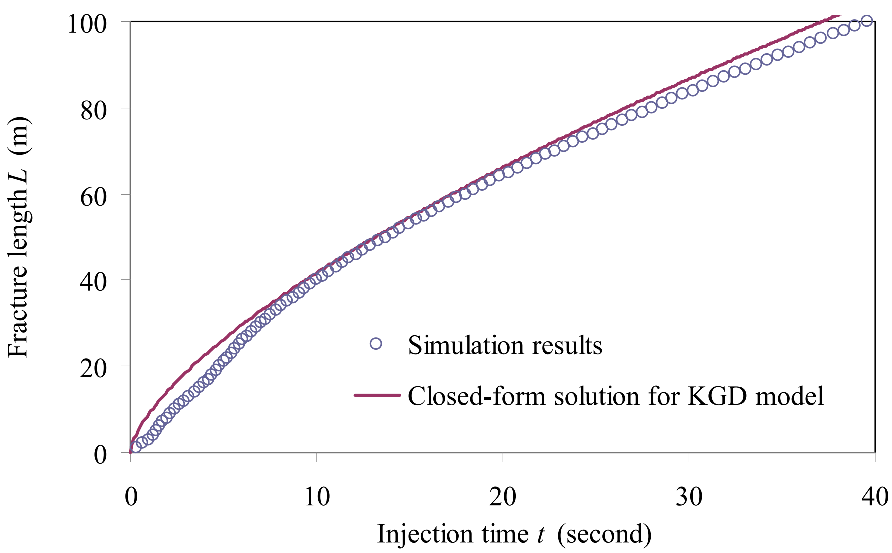

Figure 3 Length of the hydraulic fracture as a function of the injection time, a comparison between the numerical simulation results and the KGD closed-form equations.

The distributions of fluid pressure *P*, flow rate *q*, and aperture width *w* along the fracture in four selected states during the propagation when the length of the fracture *L*=25, 50, 75, and 100 m are shown in Figure 4. During the propagation of the fracture, the majority of pressure drop along the fracture between the injection well and the fracture tip takes place near the tip where the aperture size is much smaller than that near the well bore. The cross-section shape of the fracture is similar to a half-ellipse, consistent with the expectation of the KGD model. The flow rate also decreases along the fracture length, reflecting the fluid volume that is consumed by the expansion of the fracture aperture as the fracture propagates, namely the second term in equation (1). While the injection flow rate is the flow boundary condition used in the KGD model, some random fluctuation of the flow rate of q near the injection well when the fracture is short (say l=25m) is noticed in the simulation results. This is because the flow boundary condition in the simulator does not directly control the flow rate. Instead, we use a pressure-controlled boundary condition and a servomechanism to alter the pressure until the desired flow rate is reached. Such fluctuations in the beginning of the simulation are expected and the flow rate converges to the prescribed value as the simulation progresses.

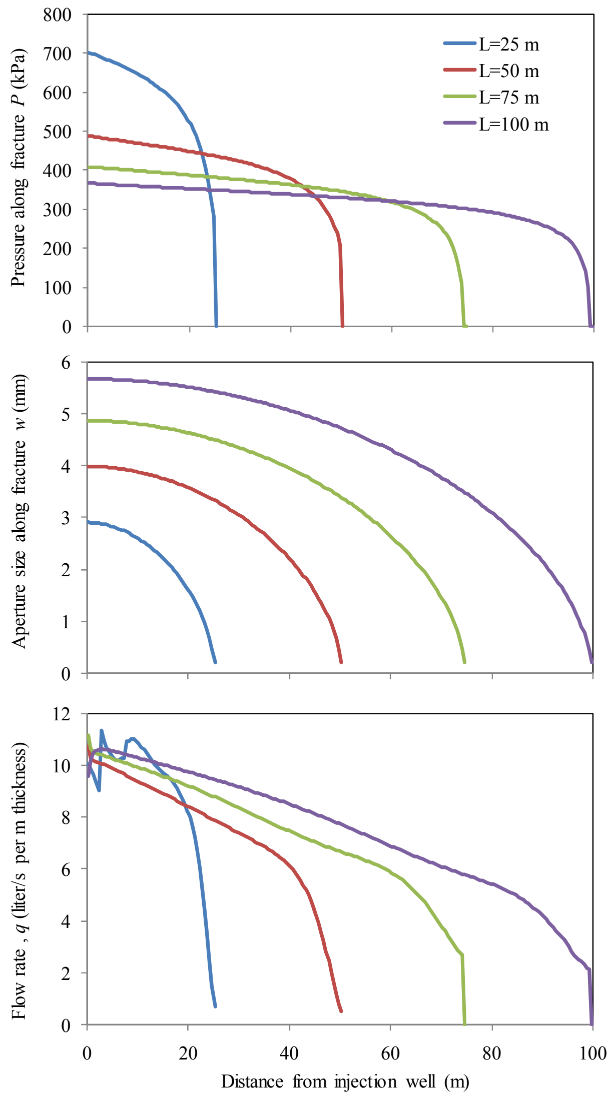

Figure 4 Distributions of P, w and q along the fracture based on the simulation results.

4. STUDY OF RESPONSES OF A RESERVOIR WITH ISOTROPICALLY ORIENTED NATURAL FRACTURES

In this section we use the numerical simulator to investigate the stimulation of a reservoir with the presence of largely isolated natural fractures with uniformly distributed orientations. The variables to be studied include the orientation of the far-field principal stress axes, the degree of stress anisotropy, and pumping pressure.

4.1. Natural Fractures and Meshing Strategy

The core simulation domain is 100 m long in each dimension (from 0 to 100 m in the *x*/horizontal direction and from -50 m to 50 m in the *y*/vertical direction), and the triangle elements have edges approximately 1 m long. The mesh is based on a regular mesh consisting of squares and the triangles are obtained by dividing the squares along their diagonals. Subsequently, a small and random perturbation is given to each node to add some randomness to the mesh as shown in Figure 5(c). Progressively large element sizes are employed to extend the simulation domain to 1,000 m in each direction, and the far field stress conditions are applied at the boundary of the extended mesh. A preexisting natural fracture system is randomly generated along the interfaces between the solid elements within the core simulation domain as shown in Figure 5(a). The fractures are largely isolated with lengths ranging from 6 m to 18 m with a mean of 11 m. The orientations of these fractures are uniformly distributed between 0 and 180 degrees rotating from the *x* direction. The injection well for hydraulic stimulation is placed at x=0 and y=0. At the bottom, top, and right boundaries of the core simulation domain, a zero-pressure boundary condition is specified in the flow solver as shown in Figure 5(b), so these three boundaries are treated as fluid "sinks".

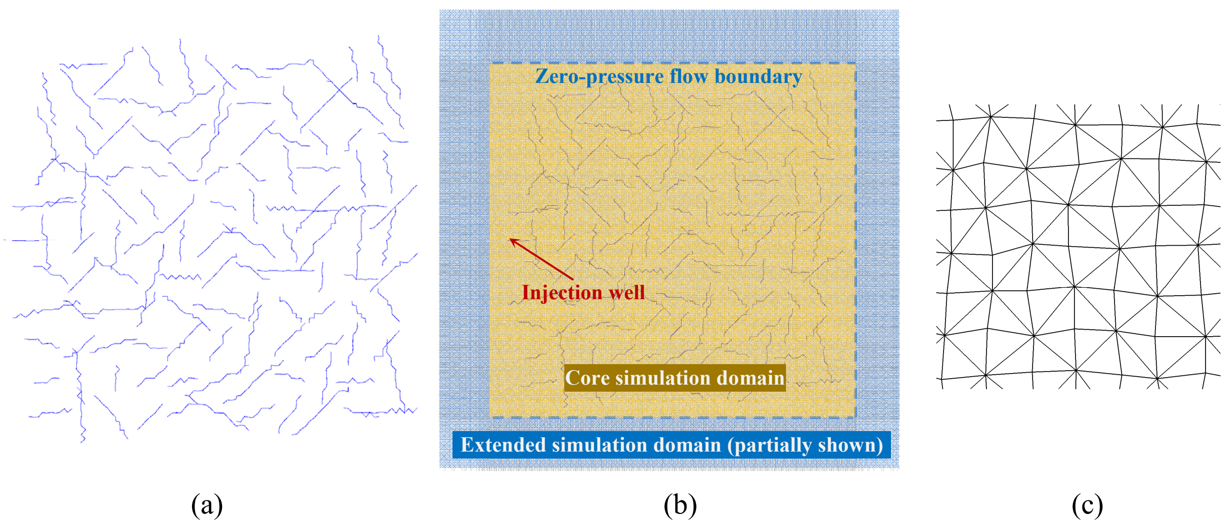

Figure 5 Preexisting natural fractures and the meshing strategy. (a) The randomly generated natural fractures; (b) the core simulation domain and the extended domain; and (c) perturbed mesh to introduce randomness to the fracture path.

4.2. The Effects of Principal Stress Orientation

Three simulations are performed in this study. In the baseline case (A-1), the far-field stress is $\sigma_{xx}= -15$ MPa, $\sigma_{yy}= -10$ MPa, and $\sigma_{xy}= 0$ (compressive stress is negative in this paper). Fluid is pumped into the system through the injection well denoted in Figure 5(b) at a constant pressure of 14 MPa. The simulation result of the stimulated fracture system for the baseline case at the end of the stimulation are shown in Figure 6(a), where the fractures (including both natural and created fractures) that are engaged (i.e. connected to the injection well and pressurized by the fluid) in the stimulation are shown in red color and the unaffected fractures are in gray. Note that the aperture widths are magnified by twenty times to enable clear visualization. The distribution of stress σ_{yy} at the end of the stimulation is shown in Figure 6(b) where the additional compressive stress created by the pressurized fractures along the horizontal direction and the tensile stress at fracture tips in the pumping front are visible. The simulation results for the two additions cases, A-2 and A-3, where the principal stresses have rotated counterclockwise and clockwise, respectively, by 30 degrees are shown in Figure 6(c) and (d).

According to classical theories of hydraulic fracturing (e.g. Huttert and Willis, 1957) in homogeneous media, hydraulic fractures should propagate along the plane of the least compressive (far-field) stress. In all three cases, the general orientations of the engaged fracture systems are consistent with the predicted directions based on the far-field principal stress orientation. In other words, the hydraulic fractures have generally propagated along the far-field least compressive stress plane. The heterogeneity in the rock body due the presence of natural fractures inevitably affects the paths along which hydraulic fractures propagate, making them deviate from the ideally predicted paths. These effects appear to be local with a minimal influence on the general trends of the fractures. Moreover, these effects, embodied by the interactions between fractures are well reflected in the numerical model.

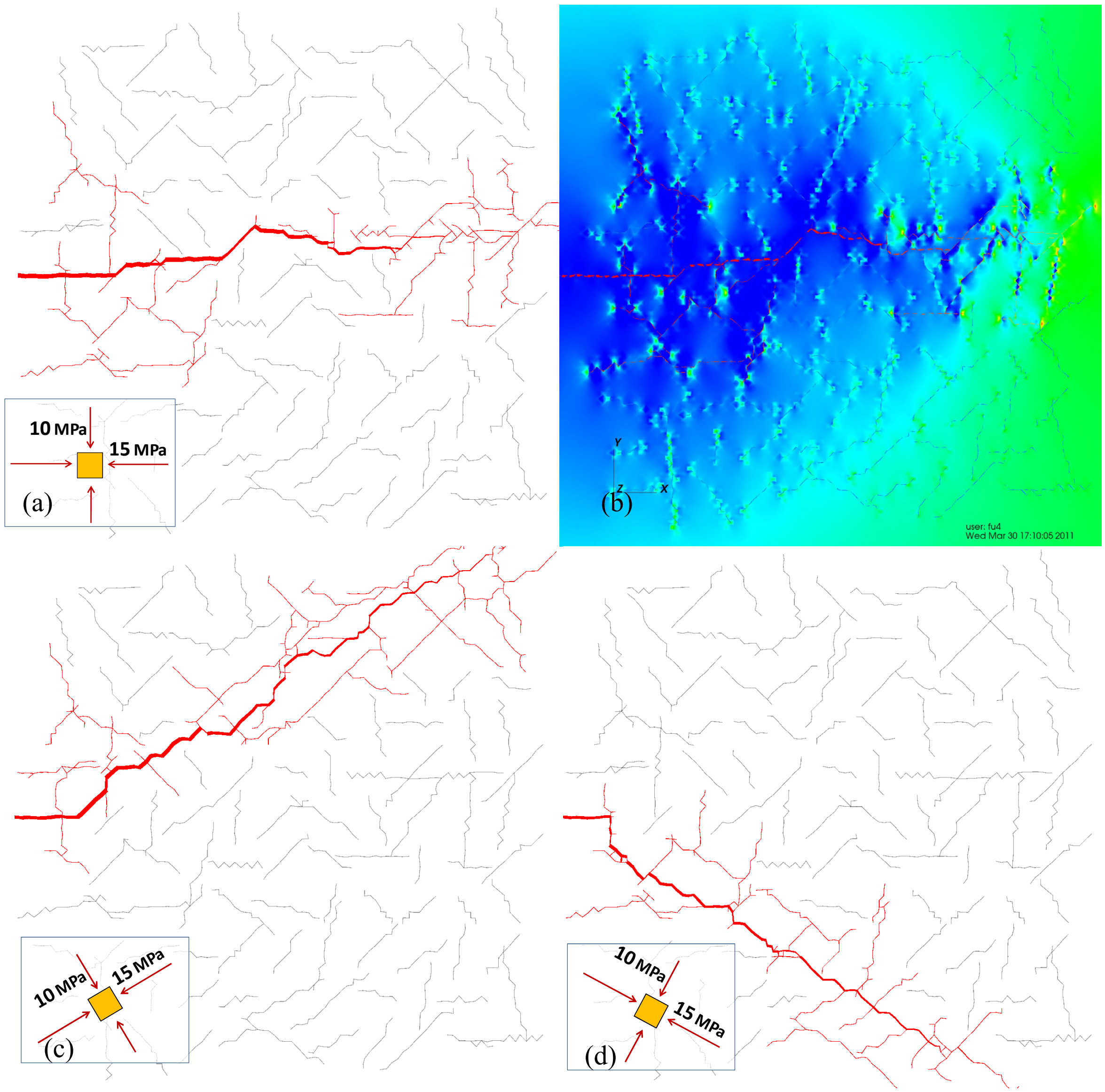

Figure 6 Stimulated fracture networks with different far-field principal stress orientations. Preexisting natural fractures and newly created fractures that are engaged by the stimulation are shown in red color, whereas unaffected natural fractures are in gray. (a) Baseline case A-1, the plane of minimum compress stress is horizontal; (b) distribution of σ_{yy} in the baseline case at the end of stimulation; (c) case A-2, the principal stresses have rotated counterclockwise by 30 degrees from the baseline; and (d) case A-3, the principal stresses have rotated clockwise by 30 degrees from the baseline.

This study also demonstrates that the mesh dependency of fracture paths (i.e. fractures can only propagate along interfaces between solid elements), which is inevitable in this class of numerical methods can be reasonably minimized by appropriate meshing strategies. In the current meshing scheme, the inter-element interfaces, namely potential fracture paths are generally along directions 0°, 45°, 90°, and 135° from the *x*-axis with some randomness introduced by the mesh perturbation. However, this does not prevent the fractures from propagating along directions 30° or 150° from the *x*-axis.

4.3. The effects of stress anisotropy

In this study, the baseline case B-1 is the same as the baseline case A-1 in Section 4.2. The additional scenarios have the same far-field vertical stress ($\sigma_{yy}= -10$ MPa) as the baseline case but smaller horizontal compressive stresses $\sigma_{yy}= -12$, -11, and -10 MPa for cases B-2, B-3, and B-4, respectively. Note that the far-field stress for case B-4 is isotropic. The pumping pressure for all the cases is 14 MPa, the same as the previous study in Section 4.2. The simulation results are shown in Figure 7 in a fashion similar to that of Figure 6, with fractures engaged in the stimulation highlighted. The result for B-1 is the same as that for A-1, and is thus not repeated in Figure 7.

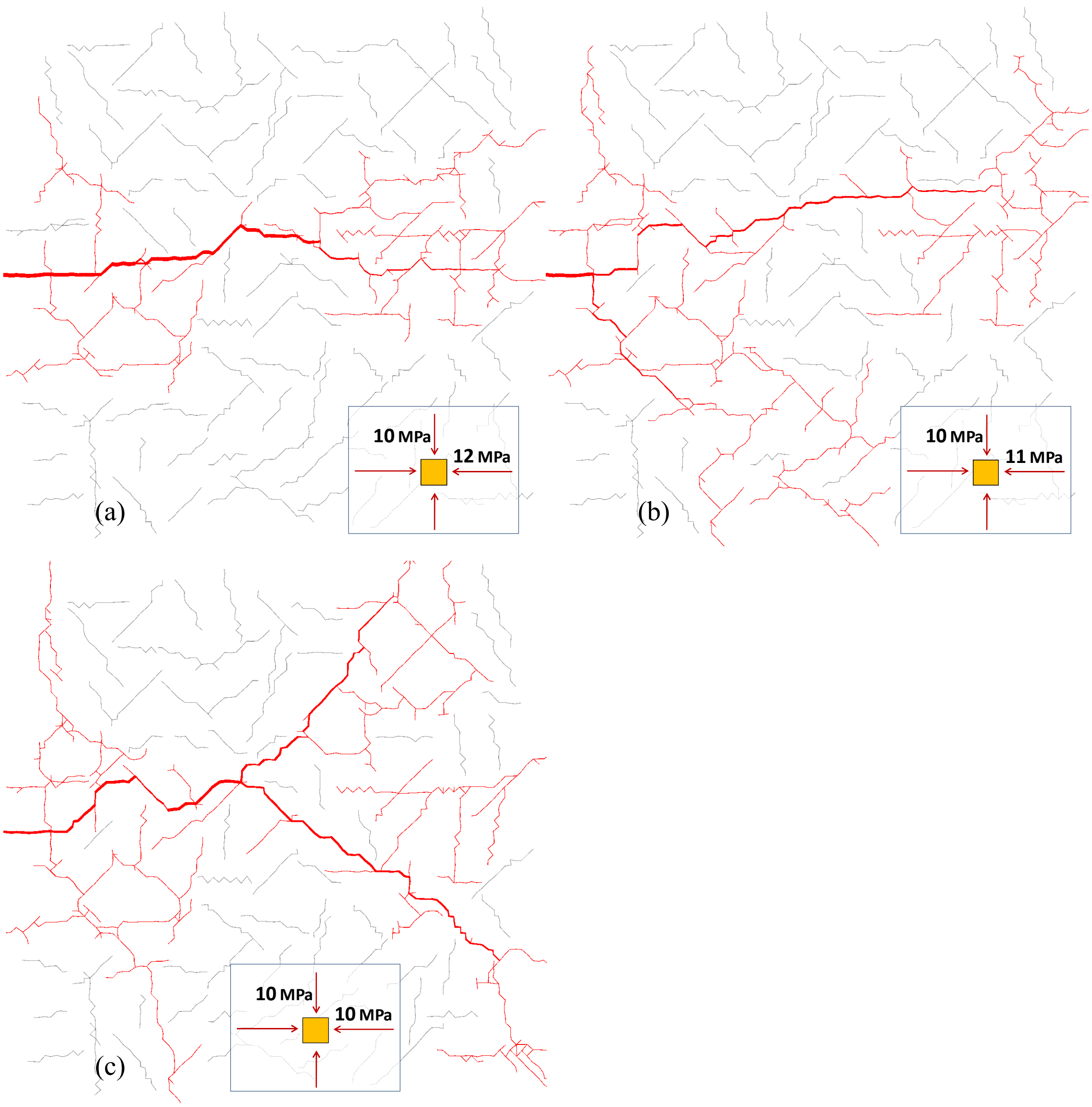

Figure 7 Stimulated fracture networks under different degrees of stress anisotropy but the same principal stress axis orientation. The far-field stress state is denoted in each figure.

The stimulated fracture network for case B-2 is similar to that of the baseline case, with slightly more scattered pattern of fracture growth at the far side from the injection well, presumably because the reduced compressive stress in the x direction gives more flexibility in the choice of viable propagation paths by the hydraulic fracture. As the compressive stress in the x direction further decrease in case B-3, another major cluster of fractures develops deviating from the primary hydraulic fracture system, propagating along the direction approximately 45 degree rotating clockwise from the x-axis. In this case, although the fractures still show preference, to some extent, for propagating along the plane with the least compressive stress, but this preference has been substantially weakened by the lesser degree of stress anisotropy. In the last case B-4, there is no preferential fracture propagation direction since the far-field stress is isotropic. Four branches of fractures have developed as the results of the stimulation along largely random directions, but these four branches tend to propagate away from each other. This is because if two parallel fractures are close to each other, the compressive stress in the rock matrix induced by the fluid pressure tends to impede the development of tensile zones at the fracture tips, making their further propagation difficult.

4.4. The effects of pumping pressure

The baseline case C-1 for this study is the same as case B-4 with isotropic far-field stress ($\sigma_{xx}= \sigma_{yy}= -10$ MPa) and a pumping pressure of 14 MPa. The two additional cases have the same far-field stress as that of the baseline case, but with lower pumping pressures, 13 MPa for case C-2, and 12 MPa for C-3. The simulation results are shown in Figure 8, and the interpretation is fairly straightforward. A higher pumping pressure will stimulate a larger fracture network during a given time period, and the stimulated network reaches farther from the well and engage more existing natural fractures. When the pumping pressure is reduced, the likelihood that a branch of the fracture will be “stuck” somewhere due to certain local features (e.g. high local compressive stress due to the influence of pressurized neighbor fractures, heterogeneity in rock properties, etc.) is increased.

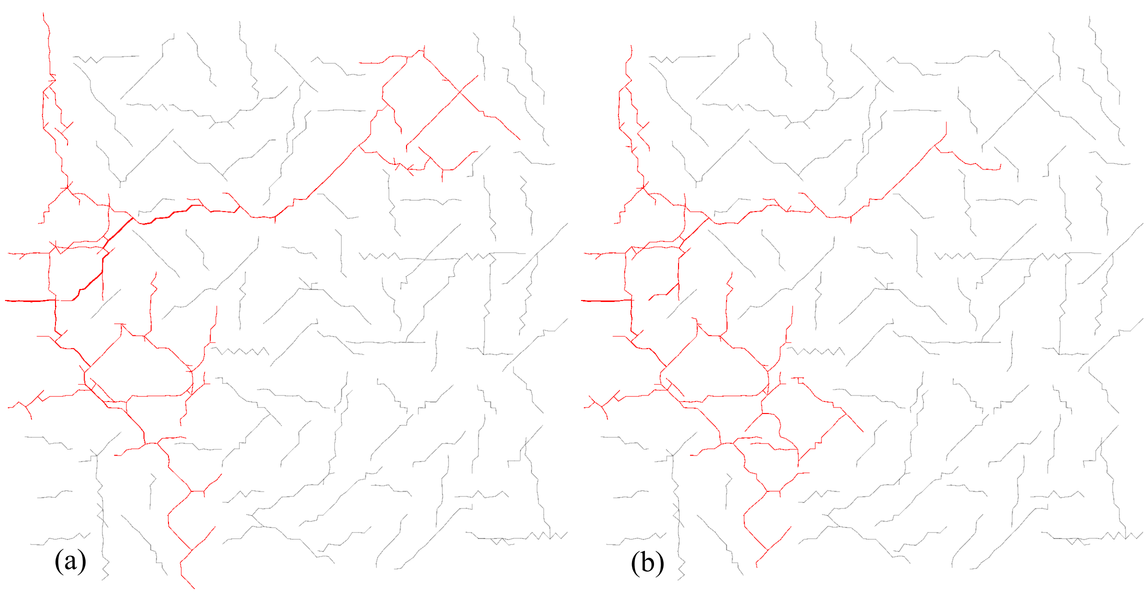

Figure 8 Stimulated fracture networks under different pumping pressures, (a) 13 MPa and (b) 12 MPa for a reservoir with isotropic far-field stress ($\sigma_{xx}= \sigma_{yy}= -10$ MPa). Note that the result for the baseline case with a 14 MPa pumping pressure is shown in Figure 7(c).

5. STUDY OF MULTI-WELL STIMULATIONS

In this section we investigate the potential benefits of stimulating a reservoir from multiple wells.

The preexisting natural fracture system in a 100 m×100 m domain is shown in Figure 9. There are two wells, Well A and Well B, at the left and right sides of the domain, respectively. Since practically neither the wells nor the fractures are entirely vertical, a well in the real world usually intersect with multiple fractures at different depths within the pay zone. To reflect this phenomenon in a 2D model, each well is represented by a finite length line segment (visualized as a narrow box in Figure 9). If a fracture intersects with the line segment, it is assumed to be connected to the well, and the appropriate pressure boundary condition is applied at the intersection points in the flow solver. In the initial state of this natural fracture system, the fractures are more or less interconnected but do not form a complete flow path bridging the two wells. The extended simulation domain around the core domain is included in the simulation but not shown in the figures.

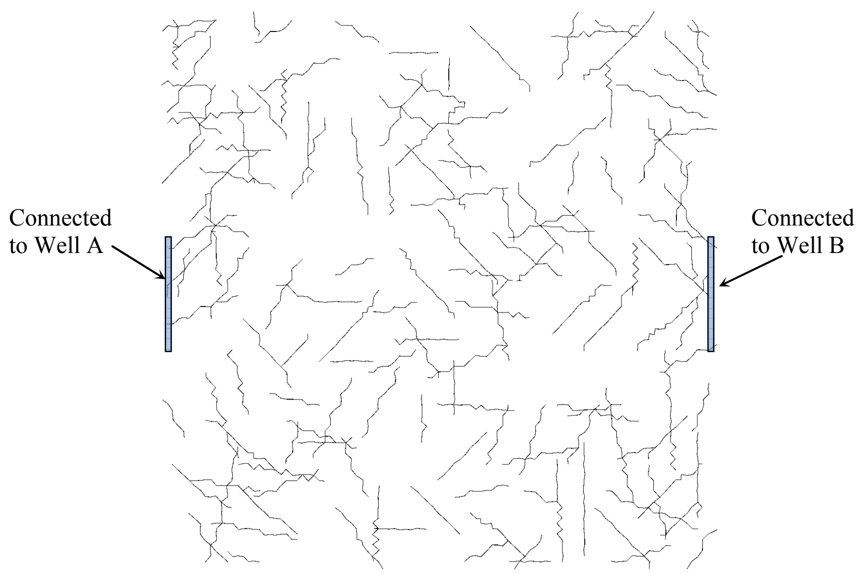

Figure 9 The natural fracture system and the locations of the two wells in this study.

In all the simulation below, the far field stress state is assumed to be $\sigma_{xx}= -13$ MPa, $\sigma_{yy}= -10$ MPa, and $\sigma_{xy}= 0$. Four stimulation scenarios are simulated:

- Case D-1, fluid is pumped into Well A based on the initial natural fracture system;
- Case D-2, fluid is pumped into Well B based on the initial natural fracture system;
- Case D-3, fluid is pumped into Well B based on the stimulated fracture system in Case D-1; and
- Case D-4, fluid is pumped into Well A based on the stimulated fracture system in Case D-2.

The stimulation pumping pressure for all the scenarios is 14 MPa.

To evaluate the permeability of the reservoir resulting from the stimulations, production stage (compared to stimulation stage) flow simulations are performed on the stimulated fracture systems. Fluid at 9 MPa pressure is injected into Well A (the injection well) and a zero-pressure flow boundary condition is applied to Well B (9 MPa pressure drop between the two wells). The simulation periods are long enough to allow the steady state to be reached. The calculated steady-state flow rates are used to back-calculate the equivalent permeability of the stimulated reservoirs.

Figure 10 shows the stimulated reservoirs for the four cases. The flow channels contributing to the permeability from the injection well to the production well are denoted in red while the other fractures in gray. It should be noted that this treatment is different from the visualization scheme used in Figure 6 to

Figure 8, where all the fractures connected to the injection well are highlighted. In a stimulated fracture network, some fractures are connected to the wells and are thus pressurized, but they are "dead ends" for flow and do not contribute to the permeability. These fractures are not highlighted in Figure 10.

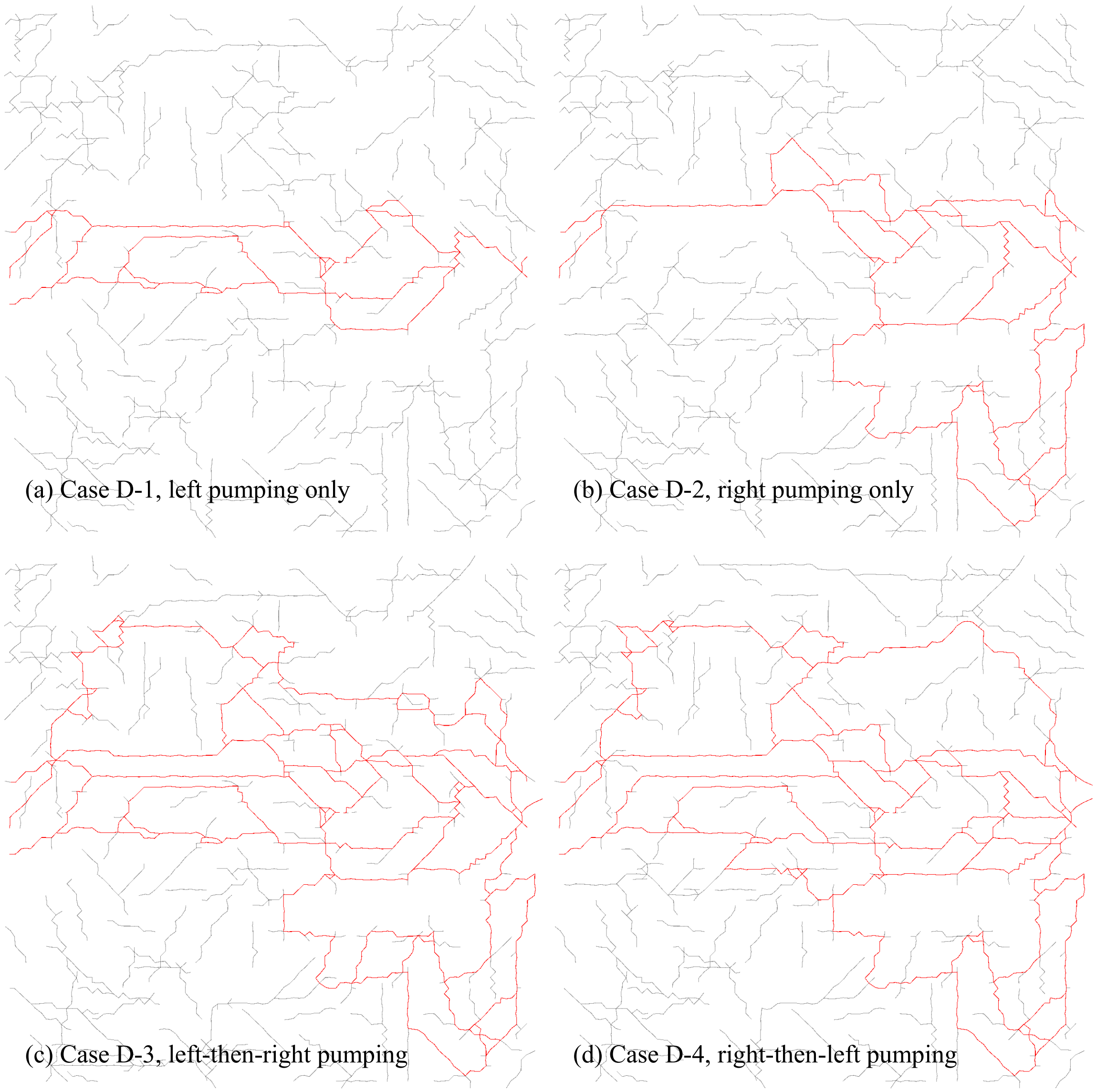

Figure 10 Stimulated fracture networks with different stimulation strategies in the multi-well stimulation study. The fractures contributing to the permeability between the two wells in the steady-flow stage are highlighted in red color.

To quantify the equivalent bulk permeability of the stimulated reservoir, two assumptions have to be made:

- The affected width (in the *y* direction) of the reservoir is 100 m, although there are portions of the simulation domain (depending on the stimulation scenario) that are not stimulated and do not contribute to the permeability.
- The average residual aperture width due to asperity of the rock surfaces along the fractures is 0.2 mm. If further investigation can provide a more accurate value of the average aperture width, the

calculated permeability value can be scaled using the cubic law (equation 3): doubling the aperture width will increase the permeability by eight times.

The calculated permeability values are 0.013, 0.011, 0.025, and 0.026 Darcy for Cases D-1, D-2, D-3, and D-4, respectively. The reservoir stimulated from Well A alone and that stimulated from Well B have similar permeability values. In both cases, additional stimulation from the second well approximately doubles the permeability. It can also be observed in Figure 10 that the additional stimulation in Case D-3 and D-4 also significantly increases the complex of the fracture network and engages a substantially larger area of the reservoir, which are particularly attractive for geothermal applications. However, the quantitative effects of these stimulation strategies on the thermal performance of this enhanced geothermal system are to be investigated by employing the Non-isothermal Unsaturated Flow and Transport (NUFT), another LLNL code, as described in Johnson et al. (2010) and Fu et al. (2011a).

6. CONCLUDING REMARKS

In this study we use a numerical test bed to investigate the stimulation-response relationships for complex fracture systems in enhanced geothermal reservoirs. Compared to other analytical and numerical models, the most important feature of the proposed numerical simulator is its capability of effectively handling the complex interactions between individual fractures in a fracture network. We have shown the simulation results of a number of relatively simple stimulation scenarios, for which either close-form solutions exist or the outcomes can be estimated based on simple principles. After establishing the credibility of the numerical test bed, we studied some relatively complex stimulation scenarios involving multiple wells to demonstrate the potential applications of the method. Note that the effects of hydraulic stimulation are highly dependent on the characteristics of the natural fracture system as well as the *in situ* stress states, so the effectiveness of different stimulation strategies has to be evaluated on a case-by-case basis and cannot be simply extrapolated based on the limited analysis on particular assumed fracture systems presented in this study. This paper documents our ongoing research effort in developing the numerical test bed for EGS applications at the Lawrence Livermore National Laboratory. We are currently further improving its capability by optimizing individual modules of the simulator and enhancing the simulation efficiency.

AUSPICES AND ACKNOWLEDGMENTS

The authors gratefully acknowledge the Geothermal Technologies Program of the US Department of Energy for support of this work under the Enhanced Geothermal Systems Program. The authors also would like to acknowledge their collaborators at the Lawrence Livermore National Laboratory. This work was performed under the auspices of the U.S. Department of Energy by Lawrence Livermore National Laboratory under Contract DE-AC52-07NA27344. This manuscript was approved to be released by LLNL with a release number LLNL-CONF-482708.

REFERENCES

Adachi J., E. Siebrits, A. Peirce, and J. Desroches, 2007. “Computer simulation of hydraulic fractures.” *International Journal of Rock Mechanics and Mining Sciences*, 44: 739-757.

Barton N., S. Bandis, and K. Bakhtar, 1985. "Strength, deformation and conductivity coupling of rock joints." *International Journal of Rock Mechanics and Mining Sciences & Geomechanics Abstracts*, 22: 121-140.

Camacho G., and M. Ortiz, 1996. "Computational modelling of impact damage in brittle materials." *International Journal of Solids and Structures*, 33: 2,899-2,938.

Dahi-Taleghani, A., 2009. *Analysis of Hydraulic Fracture Propagation in Fractured Reservoirs : An Improved Model for the Interaction Between Induced and Natural Fractures*. Doctoral dissertation, the University of Texas, Austin.

Fisher M., C. Wrigh, B. Davidson, A.K. Goodwin, E.O. Fielder, W.S. Buckler, and N.P. Steinsberger, 2005. "Integrating fracture-mapping technologies to improve stimulations in the Barnett Shale." SPE Production & Facilities, 20(2): 85-93.

Fu P., S.M. Johnson, Y. Hao, and C.R. Carrigan, 2011a. "Fully coupled geomechanics and discrete flow network modeling of hydraulic fracturing for geothermal applications." *Proceedings of the 36th Stanford Geothermal Workshop*, Stanford, CA, Jan. 31 – Feb. 2, 2011.

Fu, P., J.M. Johnson, and C.R. Carrigan, 2011b. "Simulating complex fracture systems in geothermal reservoirs using an explicitly coupled hydro-geomechanical model. In the *Proceedings of the 45th US Rock Mechanics/Geomechanics Symposium*, paper #11-244, June 26-29, San Francisco, CA.

Geertsma J., and F. de Klerk, 1969. "A rapid method of predicting width and extent of hydraulically induced fractures." *Journal of Petroleum Technology*, 21: 1,571-1,581.

Huttert K.M., and D.G. Willis, 1957. "Mechanics of hydraulic fracturing." *Transactions of the American Institute of Mining And Metallurgical Engineers*, 210: 153-163.

Johnson S.M., and J.P. Morris, 2009. "Modeling hydraulic fracturing for carbon sequestration applications." *Proceedings of the 43rd US Rock Mechanics Symposium and the 4th US-Canada Rock Mechanics Symposium,* Asheville, NC, ARMA 09-30.

Johnson S.M., Y. Hao, and L. Chiaramonte, 2010. "Upscaling of thermal transport properties in enhanced geothermal systems." *Fall Meeting of the American Geophysical Union*, San Francisco, CA, Dec. 12-17.

Khristianovic S.A., and Y.P. Zheltov, 1955. "Formation of vertical fractures by means of highly viscous liquid." *Proceedings of the Fourth World Petroleum Congress*, Rome, 579–86.

King G., L. Haile, J. Shuss, and T. Dobkins, 2008. "Increasing fracture path complexity and controlling downward fracture growth in the Barnett Shale." *Proceedings of SPE Shale Gas Production Conference,* paper number 119896-MS, 16-18 November 2008, Fort Worth, Texas.

MIT, 2006. *The Future of Geothermal Energy: Impact of Enhanced Geothermal Systems (EGS) on the United States in the 21st Century*.

Warpinski N.R., and L.W. Teufel, 1987. "Influence of geologic discontinuities on hydraulic fracture propagation." *Journal of Petroleum Technology*, 39(2): 209-220.

Xu X.P., and A. Needleman, 1994. "Numerical simulations of fast crack growth in brittle solids." *Journal of the Mechanics and Physics of Solids*, 42: 1,397-1,434.